

Strongly coupled edge states in a graphene quantum Hall interferometer

Thomas Werkmeister^{1*}, James R. Ehrets², Yuval Ronen^{2,3}, Marie E. Wesson¹, Danial Najafabadi⁴,
Zezhu Wei^{5,6}, Kenji Watanabe⁷, Takashi Taniguchi⁸, D.E. Feldman^{5,6}, Bertrand I. Halperin²,
Amir Yacoby^{1,2}, Philip Kim^{1,2*}

¹John A. Paulson School of Engineering and Applied Sciences, Harvard University, Cambridge, MA 02138, USA

²Department of Physics, Harvard University, Cambridge, MA 02138, USA

³Department of Condensed Matter Physics, Weizmann Institute of Science, Rehovot 7610001, Israel

⁴Center for Nanoscale Systems, Harvard University, Cambridge, MA 02138, USA

⁵Department of Physics, Brown University, Providence, Rhode Island 02912, USA

⁶Brown Theoretical Physics Center, Brown University, Providence, Rhode Island 02912, USA

⁷Research Center for Functional Materials, National Institute for Materials Science, 1-1 Namiki, Tsukuba 305-0044, Japan

⁸International Center for Materials Nanoarchitectonics, National Institute for Materials Science, 1-1 Namiki, Tsukuba 305-0044, Japan

*e-mail: werkmeister@g.harvard.edu; pkim@physics.harvard.edu

Electronic interferometers using the chiral, one-dimensional (1D) edge channels of the quantum Hall effect (QHE) can demonstrate a wealth of fundamental phenomena. The recent observation of phase jumps in a Fabry-Pérot (FP) interferometer revealed anyonic quasiparticle exchange statistics in the fractional QHE. When multiple integer edge channels are involved, FP interferometers have exhibited anomalous Aharonov-Bohm (AB) interference frequency doubling, suggesting putative pairing of electrons into $2e$ quasiparticles. Here, we use a highly tunable graphene-based QHE FP interferometer to observe the connection between interference phase jumps and AB frequency doubling, unveiling how strong repulsive interaction between edge channels leads to the apparent pairing phenomena. By tuning electron density *in-situ* from filling factor $\nu < 2$ to $\nu > 7$, we tune the interaction strength and observe periodic interference phase jumps leading to AB frequency doubling. Our observations demonstrate that the combination of repulsive interaction between the spin-split $\nu = 2$ edge channels and charge quantization is sufficient to explain the frequency doubling, through a near-perfect charge screening between the localized and extended edge channels. Our results show that interferometers are sensitive probes of microscopic interactions and enable future experiments studying correlated electrons in 1D channels using density-tunable graphene.

1 INTRODUCTION

2 Electrons in 1D quantum systems exhibit striking phenomena, including the breakdown of Fermi liquid
3 theory and quasiparticle formation in favor of collective modes¹. Likewise, electrons confined to two dimensions and
4 subjected to perpendicular magnetic fields exhibit the quantum Hall effects (QHEs)². Although the microscopic details
5 of QHE states are still an active area of research^{3,4}, their low-energy transport properties are known to be governed by
6 chiral, 1D edge channels⁵⁻⁸. These edge channels (ECs) conduct charge ballistically, allowing for phase-coherent
7 electronic experiments^{9,10}. In particular, electronic Fabry-Pérot (FP) QHE interferometry¹¹⁻¹³, was performed
8 extensively in GaAs, culminating in the observation of interference phase jumps as evidence for anyonic statistics of
9 fractional quasiparticles¹⁴⁻¹⁷. Recently, FPs were developed in graphene, which showed Aharonov-Bohm (AB)

10 interference of integer ECs^{18–20}, with oscillation periodicity set by the magnetic flux quantum for electrons $\Phi_0 \equiv h/e$.
11 Our previous design¹⁸ utilized graphite gates encapsulating the graphene channel, which screened bulk charges.
12 Without such screening layers²¹, however, interferometers exhibit ‘Coulomb dominated’ (CD) behavior in which
13 strong coupling of the interfering EC to localized compressible states in the bulk determines the oscillation periodicity
14 and obscures the expected AB oscillations^{13,22–24}.

15 When bulk charges were strongly screened, GaAs FPs showed unexpected doubling of the AB oscillation
16 frequency and shot noise corresponding to charge $2e$ when interfering the outermost EC with the bulk of the
17 interferometer in filling $2.5 \leq \nu \leq 4.5$, suggesting a possibility of ‘pairing’ of elementary charges²⁵. Furthermore, the
18 coherence and periodicity of the interfering outer EC were related to the coherence and the enclosed flux of the
19 adjacent inner EC²⁶, and the ‘pairing’ phenomena only occurred when the outer two modes belonged to the same spin-
20 split Landau level²⁷. Independently, single-electron capacitance measurements in GaAs quantum dots revealed that
21 tunneling into the edge of the dot corresponded to the entrance of two electrons rather than one for $\nu \geq 2$, and that
22 near $\nu \approx 2.5$ the charging peaks follow doubled magnetic flux frequency²⁸. Mechanisms of electron pairing are
23 important questions in emergent phenomena, e.g. high-temperature superconductivity²⁹ and the $\nu = 5/2$ fractional
24 QHE state in GaAs³⁰ and bilayer graphene^{31,32}. However, theoretical work concerning FP interferometers was able to
25 explain the doubled AB oscillation frequency based on a microscopic model without explicit introduction of electron
26 pairing, though explaining other related phenomena in GaAs remains challenging³³.

27 In this work, we experimentally address the microscopic mechanism of coupling between QHE edges by
28 elucidating the relation between AB oscillation phase jumps and frequency doubling, employing a highly tunable QHE
29 FP interferometer with strongly screened bulk charge in graphene. **We observe periodically modulating interference**
30 **phase jumps on the outer EC leading to nearly doubled AB oscillation frequency as we increase the electron density**
31 **in-situ**, unveiling a density-induced transition which was not explored in GaAs. We find that strong repulsive
32 **interactions between the outermost pair of spin-split ECs can explain both the observation of interference phase jumps**
33 **and the approximately doubled interference frequency**.

34 **RESULTS**

35 **Interferometer design and tuning**

36 We designed a graphene-based FP interferometer tuned by a local gate array (Fig. 1a). The FP cavity is
 37 defined electrostatically using separated graphite top-gates (Methods and [Supplementary Fig. 1](#)), which ensure a high
 38 [channel quality and allow a high degree of density tunability in-situ](#). Metal bridges contact each top-gate, and we
 39 additionally suspend metal bridges over the two quantum point contacts (QPCs), illustrated in Fig. 1b. By applying
 40 voltages V_{QPC1} and V_{QPC2} to these suspended bridge gates, we can tune [the transmission](#) of each QPC independently
 41 while keeping the filling factor of the surrounding regions fixed ([Supplementary Section 1](#)).

42 In our experiments, we measure the diagonal conductance G_D , as defined in Fig. 1b. In the regime that we
 43 study, $G_D = \frac{e^2}{h} \nu_{QPC}$ where ν_{QPC} counts the number of edge channels transmitted through the device, with a partially
 44 transmitted channel counted as fraction^{34,35}. To characterize the QPC transmissions, we measure G_D as a function of
 45 the bottom-gate voltage and split-gate voltage for each QPC with the bulk of the interferometer tuned to $\nu = 2$ at $B =$
 46 6 T ([Supplementary Fig. 3](#)). At $\nu = 2$, there are two spin-split Landau levels, of which the lower energy spin species
 47 hosts an EC closer to the effective boundary of the sample. Hence, we refer to the EC belonging to the lower (higher)
 48 energy spin species as the ‘outer’ (‘inner’) EC. Once appropriate bottom-gate and split-gate voltages are set, we tune
 49 V_{QPC1} and V_{QPC2} , voltages applied on the suspended bridges to control the individual QPC transmissions. Fig. 1c and
 50 Fig. 1d show the measured G_D as a function of V_{QPC1} and V_{QPC2} , respectively, with the other QPC fully open. G_D
 51 exhibits plateaus at $(0,1,2) \frac{e^2}{h}$, corresponding to (neither, outer, both) ECs transmitted. In this regime, we define
 52 $T_{QPC} \equiv G_D \frac{h}{e^2}$ as the transmission of the QPC³⁴, [where \$0 < T_{QPC} < 1\$ corresponds to a partitioned outer EC and](#)
 53 [\$1 < T_{QPC} < 2\$ corresponds to a partitioned inner EC](#).

54 Tuning to partial transmission of the inner EC for both QPCs, $T_{QPC1} = T_{QPC2} = 1.5$, we observe high-
 55 visibility conductance oscillations as a function of plunger gate voltage V_{PG} , which tunes the filling factor ν_{PG} under
 56 the plunger gate, in Fig. 1e. Similarly, we tune to $T_{QPC1} = T_{QPC2} = 0.5$ and measure conductance oscillations on the
 57 outer EC in Fig. 1f. In both cases, oscillations are largest for $\nu_{PG} < 0$, which corresponds to a fully gate-defined
 58 interference path since electrons are depleted under the gate. Increasing ν_{PG} brings the interfering edge closer to the
 59 etched graphene boundary, inducing dephasing¹⁸. Notably, the inner EC oscillations survive until $\nu_{PG} = 2$, when it
 60 flows close to the etched boundary of the graphene, while the outer EC reaches the boundary at $\nu_{PG} = 1$. Another

61 difference is the apparent irregularity of the oscillations on the outer EC compared to the inner EC, which we will
62 understand in this work.

63 **Phase jumps and AB oscillation frequency transition**

64 High-visibility oscillations allow us to probe the dependence of interference phase θ on magnetic field
65 variation δB and gate voltage variations, which distinguishes the AB from the CD regimes^{13,15,18,19,22}. For small
66 variations in field and gate voltages in the AB regime, we expect $\delta\theta/2\pi \approx A\delta B/\Phi_0 + C_{PG}\delta V_{PG}/e + C_{MG}\delta V_{MG}/e$,
67 where A , C_{PG} , and C_{MG} , are the (approximately constant) area enclosed by the interfering EC, interfering EC – plunger
68 gate capacitance, and interfering EC – middle gate capacitance, respectively. Importantly, V_{MG} also directly tunes the
69 electron density in the interferometer, namely sweeping V_{MG} over a large range will change the FP cavity filling factor
70 v_{MG} . To calibrate the filling that we expect in the cavity, we first measure standard Hall conductance in the region
71 gated by V_{LG} (see Supplementary Fig. 1e) and observe conductance plateaus (Fig. 2a). Since the top gates are
72 identically coupled to the channel directly beneath them, an identical sweep of V_{MG} will tune v_{MG} through the same
73 filling factors. Data in the remaining panels of Fig. 2 were taken with the QPCs set to $T_{QPC1} = T_{QPC2} = 0.5$ i.e.
74 partitioning the outer EC. Near the lowest density of the $v_{MG} = 2$ plateau (Fig. 2b), we observe a typical AB
75 interference pattern. Constant phase stripes ($\delta\theta = 0$) trace out a negative slope $\delta V_{PG}/\delta B$ with magnetic field period
76 ΔB yielding $\Phi_0/\Delta B = 1.13 \mu\text{m}^2$, matching the designed area $A = 1.16 \mu\text{m}^2$. Plunger gate period ΔV_{PG} yields
77 $1/\Delta V_{PG} = 19.2 \text{ V}^{-1}$. Increasing v_{MG} using V_{MG} reveals more complicated interference patterns in Fig. 2c-d. Periodic
78 shifts in the interference pattern persist and modulate until near the center of $v_{MG} = 4$, as seen in Fig. 2e, when a
79 simple stripe pattern returns. However, now $\Phi_0/\Delta B = 2.32 \mu\text{m}^2$ and $1/\Delta V_{PG} = 36.3 \text{ V}^{-1}$, both approximately
80 doubled from Fig. 2b. Since A is fixed, a doubling of $\Phi_0/\Delta B$ indicates oscillations with $\Phi_0/2 = h/2e$ periodicity
81 instead of Φ_0 so that $\Phi_0/2\Delta B = 1.16 \mu\text{m}^2$. Similarly, assuming a fixed C_{PG} , then $1/\Delta V_{PG}$ doubling corresponds to
82 adding twice as many electrons to the system per flux quanta. Both could be interpreted as an effective charge $e^* =$
83 $2e$ for the interfering particle, as interpreted in GaAs²⁵⁻²⁷, but our observations indicate a different interpretation.

84 Importantly, we observe the entire density-tuned transition to the AB frequency-doubled regime at fixed B
85 by sweeping V_{MG} and observing oscillations with V_{PG} , as shown in Fig. 2f. Remarkably, the frequency transition occurs
86 continuously. From the top panel, Φ_0 interference is apparent. As V_{MG} increases, periodic phase jumps begin to appear.

87 Both the V_{MG} spacing and magnitude of the phase jumps increase, until eventually the most apparent periodicity
88 corresponds to $\Phi_0/2$ oscillations (i.e., doubled frequency $2\Phi_0^{-1}$).

89 To better understand the phase jumps, we use a general relation between charge and phase in FP
90 interferometers³⁶. When a single EC passes through the two constrictions with weak backscattering, the interference
91 phase seen by the device at zero temperature is $\theta = 2\pi Q + \theta_0$, mod 2π , where Q is the total electron charge (in units
92 e) in the region between the two scattering points and θ_0 is a constant for small variations in B , V_{PG} , and V_{MG} . In our
93 experimental regime, $\nu \geq 2$, we expect this relation to hold with $Q = Q_1 + Q_2$, where Q_1 is the total charge residing
94 in the lowest spin-split Landau level and Q_2 is the charge in the higher energy spin state (and also higher Landau
95 levels). Q_1 can vary continuously since the outer EC is connected to the source and drain charge reservoirs. In contrast,
96 Q_2 is required to be integer, as the corresponding energy levels are isolated through the incompressible QHE bulk. An
97 integral change in Q_2 has no observable effect on the interference signal unless it produces a non-integral change in
98 Q_1 due to Coulomb coupling between the two types of charge. Hence, we can redefine θ to include only the charge
99 Q_1 in the lowest spin-split Landau level, and the values Q_1 in the ground state of the interferometer determine θ .
100 Following similar models used to understand the CD regime^{15,24,37} and considering small changes in Q_1 and Q_2 , we
101 expand the change in ground state energy $E = K_1 \delta Q_1^2 + K_2 \delta Q_2^2 + 2K_{12} \delta Q_1 \delta Q_2$, where K_i is the charging energy
102 of the charge species i and K_{12} describes the mutual capacitive coupling between them. Energetic stability requires
103 that $|K_{12}|^2 \leq K_1 K_2$. Within this capacitive coupling model, when Q_2 increases by 1, the charge Q_1 correspondingly
104 decreases by a discrete (generically non-integral) amount ΔQ_1 to screen the added charge, leading to a phase shift
105 $\Delta\theta/2\pi = \Delta Q_1 = -K_{12}/K_1$.

106 By taking 1D fast Fourier transforms (FFTs) along lines parallel to the phase jumps^{14,15}, we extract several
107 values of $\Delta\theta/2\pi$ near the center of the periodicity transition in Fig. 3a. We observe that the locations where the phase
108 jumps occur (marked in Fig. 3b) follow a steeper slope than the slope $\delta V_{PG}/\delta V_{MG}$ of constant phase lines of the main
109 interference oscillation in the V_{MG} - V_{PG} planes. A steeper slope also occurs in the B - V_{PG} plane (Fig. 2c-d). Moreover,
110 these phase jump lines have negative slopes $\delta V_{PG}/\delta B < 0$, like the constant phase lines of AB oscillations. This
111 observation is in sharp contrast to the phase jumps reported in the FP interferometer operated in the fractional QHE
112 regime^{14,15} or in the FP interferometer operated in the integer CD regime³⁷, where phase jump lines follow positive
113 slope $\delta V_{PG}/\delta B > 0$. The different slope suggests a different structure to the energy levels that are being populated in
114 our sample. Considering that the outer EC is partitioned at the QPCs, while the inner ECs are well isolated, we

115 hypothesize that the charging events seen as phase jumps represent charge added to the annular, closed inner EC,
116 illustrated in Fig. 3. The dominant coupling K_{12} is directly between the outer and inner $v = 2$ ECs. Any charges added
117 to higher Landau levels or to localized states in the bulk are not measurably coupled to the outer EC, presumably
118 because of effective screening by the gates.

119

120

121

122 **AB frequency doubling from strongly coupled QHE edge states**

123 We provide further evidence for capacitively coupled QHE edges tuning the AB frequency in Fig. 4. At fixed
124 V_{MG} in the transition regime, we compare interference in the B - V_{PG} plane for the inner EC, Fig. 4a, to the outer EC,
125 Fig. 4b. This direct comparison is only possible because we can control QPC transmissions independently of bulk
126 filling. We observe that the slope of the oscillation maxima on the inner EC (dotted lines in Fig. 4a) matches the slope
127 of the phase jump lines on the outer EC (dotted lines in Fig. 4b). Reducing the transmission for the inner EC, the
128 interference maxima in Fig. 4a become sharper charging resonances, corresponding to charge $Q_2 \rightarrow Q_2 + 1$ through
129 the inner EC. When the transmission of the inner EC vanishes, the inner EC is fully disconnected from the source and
130 drain charge reservoirs, and the outer EC is now partitioned at the QPCs to form a new interference path (shown in
131 the left panel in Fig. 4b). Since the electrostatic configurations for Fig. 4a and Fig. 4b are identical, the regions in
132 between the phase jump lines in Fig. 4b correspond to fixed Q_2 , and we see that the interference phase on the outer
133 EC shifts when the charge on the inner EC discretely changes.

134 Taking Fourier transform of the interference signal provides further understanding of interactions between
135 the two ECs involved in the interference. The bottom panels of Fig. 4a and 4b show the 2D FFTs of the corresponding
136 interference patterns in the B - V_{PG} planes. For interference of the inner EC (Fig. 4a), we observe a simple FFT
137 pattern of peaks corresponding to the fundamental frequency of the inner EC \mathbf{f}_i , a vector containing the peak position
138 in the 2D FFT, and its harmonics ($n\mathbf{f}_i$, where n is an integer). The FFT pattern of the outer EC interference (Fig. 4b)
139 exhibits a more complicated lattice of Fourier peaks. If we label one of the dominant peaks as the fundamental
140 frequency of the outer EC, \mathbf{f}_o , we can then identify the rest of the peaks by addition or subtraction of the same vector
141 \mathbf{f}_i evident in the inner EC data. The lowest order peaks correspond to the sum $\mathbf{f}_{o+i} = \mathbf{f}_o + \mathbf{f}_i$ and the difference

142 $\mathbf{f}_{o-i} = \mathbf{f}_o - \mathbf{f}_i$. We show a similar Fourier lattice construction in [Supplementary](#) Fig. 5 for interference in the B - V_{MG}
143 plane.

144 By tuning V_{MG} , we modulate the filling factor of the interferometer cavity in a wide range and observe the
145 evolution of the interference patterns and corresponding peaks for the outer (inner) EC in [Supplementary](#) Fig. 2 (3).
146 As in Fig. 2, phase jumps appear only within the periodicity transition. Fig. 4c shows the magnitude of individual
147 phase jumps as a function of V_{MG} . We find that the phase jump continuously evolves from $\Delta\theta/2\pi \approx 0$ ($V_{MG} < 0.6$ V)
148 through the periodicity transition to $\Delta\theta/2\pi \approx -1$ ($V_{MG} > 1.6$ V), corresponding to the strongly coupled limit
149 $K_{12}/K_1 \approx 1$. The transition regime marked by non-trivial phase jumps spans from the appearance of the inner EC
150 ($V_{MG} \approx 0.6$ V) to the strongly coupled outer two EC limit ($V_{MG} \approx 1.6$ V).

151 The Fourier peaks' evolution tuned by V_{MG} provides insight into the interaction between ECs. Fig. 4d displays
152 the normalized Fourier peak intensity as a function of V_{MG} . The amplitude of the Fourier peak \mathbf{f}_o decays through the
153 transition regime (0.6 V $< V_{MG} < 1.6$ V), replaced by \mathbf{f}_{o+i} as the dominant peak. We [plot the magnetic field frequency](#)
154 [multiplied by \$\Phi_0\$](#) (Fig. 4e) and the plunger gate frequency (Fig. 4f), respectively, for each of the lowest-order peaks
155 \mathbf{f}_o , \mathbf{f}_i , \mathbf{f}_{o+i} , and \mathbf{f}_{o-i} as a function of V_{MG} . At the beginning of the transition regime where the ECs are not interacting,
156 both \mathbf{f}_o and \mathbf{f}_{o+i} approach the corresponding AB frequency $\Phi_0^{-1} = e/h$ through the designed area. As V_{MG} increases,
157 however, \mathbf{f}_o stays nearly unchanged, while \mathbf{f}_{o+i} increases to reach the doubled value $2\Phi_0^{-1}$. The [experimental](#)
158 [observation that the dominant peak in the frequency-doubled regime corresponds to \$\mathbf{f}_{o+i}\$](#) precludes the possibility of
159 [2e charge pairing within the outer EC alone](#).

160 Instead, our frequency-doubled regime arises from Coulomb interaction between the spin-split ECs combined
161 with charge quantization on the inner EC (Methods). Electrons would naturally tend to enter the inner EC at frequency
162 \mathbf{f}_i , but, due to charge quantization, cannot enter continuously. Hence, as the magnetic flux increases continuously, the
163 area enclosed by the inner EC must shrink to maintain fixed charge. During this shrinking process, electron charge is
164 transferred continuously into the interior, leaving missing electron charge between the outer and inner ECs. In the
165 strongly coupled EC limit, this missing charge attracts an equal charge onto the outer EC for screening. In the absence
166 of this screening effect, charge is continuously added to the outer EC with frequency \mathbf{f}_o according to the increased
167 AB phase. In the coupled ECs, the combination of the screening-induced charge and the natural AB effect results in
168 the outer EC charging at a frequency \mathbf{f}_{o+i} . Therefore, the interference phase follows \mathbf{f}_{o+i} . In addition to this continuous
169 charging effect, electrons can tunnel into the inner EC from the external reservoirs. As previously discussed, each

170 electron addition repels some electron charge from the outer EC, causing the negative interference phase shifts that
171 we observed. For larger values of V_{MG} , as the bulk density increases, the inner and outer EC move closer together, and
172 the system approaches the strong coupling limit, where the phase jumps are close to -2π and unobservable, reflecting
173 a full electron charge screening. Moreover, as the inner and outer ECs asymptotically enclose the same area, set by
174 the confining potential of the device, the frequency f_{o+i} approaches $2\Phi_0^{-1}$.

175 Note: a concurrent work also observed apparent AB frequency tripling, corresponding to the sum of the three
176 $\nu = 3$ edge channel frequencies³⁸. The framework that we developed here can be expected to naturally explain this
177 observation, since in devices utilizing the graphene crystal edge, the sharp confining potential can lead to multiple
178 ECs developing within a few magnetic lengths of the edge.⁸ The combination of reduced spatial separation and reduced
179 screening by nearby graphite gates may account for the observation of apparent tripling, arising from the outer EC
180 screening both internal localized ECs.

181

182 DISCUSSION

183 We have investigated phase jumps and AB frequency modulation in a highly tunable graphene QHE FP
184 interferometer with coupled co-propagating edge modes. We identify that interference phase jumps are related to the
185 single electron charging events in the inner EC, and the transition of the AB frequency can be connected to the
186 corresponding screening effect of the outer EC. As V_{MG} increases, the EC coupling becomes strong and the AB
187 frequency doubles, indicating a near-perfect screening between the ECs. Thus, our experimental observation supports
188 the proposal that AB frequency doubling can be explained without explicitly introducing electron pairing within the
189 outer two ECs³³. In other words, a half flux quantum introduced in the two strongly coupled ECs can bring a full
190 charge from the external reservoir and a 2π evolution of the observed interferometer phase.

191 Our observations do not exclude the possibility of further correlation effects in the strongly coupled ECs;
192 instead, the tunably coupled ECs discovered here provide a system to test the emergence of electron correlations in
193 1D systems³⁹. However, AB frequency multiplication, which we explained within a single particle picture, cannot
194 substantiate the correlation effect. Further experiments probing the transition from the weakly to strongly coupled
195 limit, such as shot noise^{25,40,41}, finite-bias dependence^{15,42}, energy relaxation⁴³, and high-frequency transport⁴⁴⁻⁴⁶ will
196 provide further insight into the ground state and excitations. More generally, inter-edge screening could affect
197 interferometry in fractional fillings containing multiple ECs^{42,47-49}, and [the recent observation of fractional interference](#)

198 in similar bilayer and monolayer graphene devices^{50–52} will enable further experiments to probe the interacting co-
199 propagating fractional QHE edge modes.

200

201

202

203

204

205

206

207

208

209

210

211

212 **References**

- 213 1. Giamarchi, T. *Quantum Physics in One Dimension*. (Clarendon Press, 2003).
- 214 2. Wen, X.-G. *Quantum Field Theory of Many-Body Systems: From the Origin of Sound to an Origin of*
215 *Light and Electrons*. (Oxford University Press, Oxford, New York, 2007).
- 216 3. Marguerite, A. *et al.* Imaging work and dissipation in the quantum Hall state in graphene. *Nature*
217 **575**, 628–633 (2019).
- 218 4. Uri, A. *et al.* Nanoscale imaging of equilibrium quantum Hall edge currents and of the magnetic
219 monopole response in graphene. *Nat. Phys.* **16**, 164–170 (2020).
- 220 5. Halperin, B. I. Quantized Hall conductance, current-carrying edge states, and the existence of
221 extended states in a two-dimensional disordered potential. *Phys. Rev. B* **25**, 2185–2190 (1982).
- 222 6. Chklovskii, D. B., Shklovskii, B. I. & Glazman, L. I. Electrostatics of edge channels. *Phys. Rev. B* **46**,
223 4026–4034 (1992).

224 7. Kim, S. *et al.* Edge channels of broken-symmetry quantum Hall states in graphene visualized by
225 atomic force microscopy. *Nat Commun* **12**, 2852 (2021).

226 8. Coissard, A. *et al.* Absence of edge reconstruction for quantum Hall edge channels in graphene
227 devices. *Science Advances* **9**, eadf7220 (2023).

228 9. Ji, Y. *et al.* An electronic Mach–Zehnder interferometer. *Nature* **422**, 415–418 (2003).

229 10. Bocquillon, E. *et al.* Electron quantum optics in ballistic chiral conductors. *Annalen der Physik* **526**,
230 1–30 (2014).

231 11. van Wees, B. J. *et al.* Observation of zero-dimensional states in a one-dimensional electron
232 interferometer. *Phys. Rev. Lett.* **62**, 2523–2526 (1989).

233 12. de C. Chamon, C., Freed, D. E., Kivelson, S. A., Sondhi, S. L. & Wen, X. G. Two point-contact
234 interferometer for quantum Hall systems. *Phys. Rev. B* **55**, 2331–2343 (1997).

235 13. Halperin, B. I., Stern, A., Neder, I. & Rosenow, B. Theory of the Fabry-P\'erot quantum Hall
236 interferometer. *Phys. Rev. B* **83**, 155440 (2011).

237 14. Nakamura, J., Liang, S., Gardner, G. C. & Manfra, M. J. Direct observation of anyonic braiding
238 statistics. *Nat. Phys.* **16**, 931–936 (2020).

239 15. Nakamura, J., Liang, S., Gardner, G. C. & Manfra, M. J. Impact of bulk-edge coupling on
240 observation of anyonic braiding statistics in quantum Hall interferometers. *Nat Commun* **13**, 344
241 (2022).

242 16. Carrega, M., Chirolli, L., Heun, S. & Sorba, L. Anyons in quantum Hall interferometry. *Nat Rev Phys*
243 **3**, 698–711 (2021).

244 17. Feldman, D. E. & Halperin, B. I. Fractional charge and fractional statistics in the quantum Hall
245 effects. *Rep. Prog. Phys.* **84**, 076501 (2021).

246 18. Ronen, Y. *et al.* Aharonov–Bohm effect in graphene-based Fabry–P\'erot quantum Hall
247 interferometers. *Nat. Nanotechnol.* **16**, 563–569 (2021).

248 19. D\'eprez, C. *et al.* A tunable Fabry–P\'erot quantum Hall interferometer in graphene. *Nat. Nanotechnol.*
249 **16**, 555–562 (2021).

250 20. Fu, H. *et al.* Aharonov–Bohm Oscillations in Bilayer Graphene Quantum Hall Edge State Fabry–
251 Pérot Interferometers. *Nano Lett.* **23**, 718–725 (2023).

252 21. Zhao, L. *et al.* Graphene-Based Quantum Hall Interferometer with Self-Aligned Side Gates. *Nano*
253 *Lett.* **22**, 9645–9651 (2022).

254 22. Zhang, Y. *et al.* Distinct signatures for Coulomb blockade and Aharonov-Bohm interference in
255 electronic Fabry-Perot interferometers. *Phys. Rev. B* **79**, 241304 (2009).

256 23. Ofek, N. *et al.* Role of interactions in an electronic Fabry–Perot interferometer operating in the
257 quantum Hall effect regime. *Proceedings of the National Academy of Sciences* **107**, 5276–5281
258 (2010).

259 24. Sivan, I. *et al.* Observation of interaction-induced modulations of a quantum Hall liquid’s area. *Nat*
260 *Commun* **7**, 12184 (2016).

261 25. Choi, H. K. *et al.* Robust electron pairing in the integer quantum hall effect regime. *Nat Commun* **6**,
262 7435 (2015).

263 26. Sivan, I. *et al.* Interaction-induced interference in the integer quantum Hall effect. *Phys. Rev. B* **97**,
264 125405 (2018).

265 27. Biswas, S., Kundu, H. K., Umansky, V. & Heiblum, M. Electron Pairing of Interfering Interface-
266 Based Edge Modes. *Phys. Rev. Lett.* **131**, 096302 (2023).

267 28. Demir, A. *et al.* Correlated Double-Electron Additions at the Edge of a Two-Dimensional Electronic
268 System. *Phys. Rev. Lett.* **126**, 256802 (2021).

269 29. Keimer, B., Kivelson, S. A., Norman, M. R., Uchida, S. & Zaanen, J. From quantum matter to high-
270 temperature superconductivity in copper oxides. *Nature* **518**, 179–186 (2015).

271 30. Willett, R. L. The quantum Hall effect at 5/2 filling factor. *Rep. Prog. Phys.* **76**, 076501 (2013).

272 31. Li, J. I. A. *et al.* Even-denominator fractional quantum Hall states in bilayer graphene. *Science* **358**,
273 648–652 (2017).

274 32. Huang, K. *et al.* Valley Isospin Controlled Fractional Quantum Hall States in Bilayer Graphene.
275 *Phys. Rev. X* **12**, 031019 (2022).

276 33. Frigeri, G. A., Scherer, D. D. & Rosenow, B. Sub-periods and apparent pairing in integer quantum
277 Hall interferometers. *EPL* **126**, 67007 (2019).

278 34. Büttiker, M. Quantized transmission of a saddle-point constriction. *Phys. Rev. B* **41**, 7906–7909
279 (1990).

280 35. Zimmermann, K. *et al.* Tunable transmission of quantum Hall edge channels with full degeneracy
281 lifting in split-gated graphene devices. *Nat Commun* **8**, 14983 (2017).

282 36. Feldman, D. E. & Halperin, B. I. Robustness of quantum Hall interferometry. *Physical Review B* **105**,
283 165310 (2022).

284 37. Röösli, M. P. *et al.* Observation of quantum Hall interferometer phase jumps due to a change in the
285 number of bulk quasiparticles. *Phys. Rev. B* **101**, 125302 (2020).

286 38. Yang, W. *et al.* Evidence for correlated electron pairs and triplets in quantum Hall interferometers.
287 Preprint at <http://arxiv.org/abs/2312.14767> (2023).

288 39. Shavit, G. & Oreg, Y. Electron pairing induced by repulsive interactions in tunable one-dimensional
289 platforms. *Phys. Rev. Res.* **2**, 043283 (2020).

290 40. Frigeri, G. A. & Rosenow, B. Electron pairing in the quantum Hall regime due to neutralon
291 exchange. *Phys. Rev. Research* **2**, 043396 (2020).

292 41. Inoue, H. *et al.* Charge Fractionalization in the Integer Quantum Hall Effect. *Phys. Rev. Lett.* **112**,
293 166801 (2014).

294 42. Wei, Z., Feldman, D. E. & Halperin, B. I. Quantum Hall interferometry at finite bias with multiple
295 edge channels. *arXiv.org* <https://arxiv.org/abs/2405.05486v1> (2024).

296 43. Altimiras, C. *et al.* Non-equilibrium edge-channel spectroscopy in the integer quantum Hall regime.
297 *Nature Phys* **6**, 34–39 (2010).

298 44. Bocquillon, E. *et al.* Separation of neutral and charge modes in one-dimensional chiral edge channels.
299 *Nat Commun* **4**, 1839 (2013).

300 45. Freulon, V. *et al.* Hong-Ou-Mandel experiment for temporal investigation of single-electron
301 fractionalization. *Nat Commun* **6**, 6854 (2015).

302 46. Hashisaka, M., Hiyama, N., Akiho, T., Muraki, K. & Fujisawa, T. Waveform measurement of
303 charge- and spin-density wavepackets in a chiral Tomonaga–Luttinger liquid. *Nature Phys* **13**, 559–
304 562 (2017).

305 47. Willett, R. L. *et al.* Interference Measurements of Non-Abelian $\$e/4\$$ & Abelian $\$e/2\$$ Quasiparticle
306 Braiding. *Phys. Rev. X* **13**, 011028 (2023).

307 48. Kundu, H. K., Biswas, S., Ofek, N., Umansky, V. & Heiblum, M. Anyonic interference and braiding
308 phase in a Mach-Zehnder interferometer. *Nat. Phys.* **19**, 515–521 (2023).

309 49. Nakamura, J., Liang, S., Gardner, G. C. & Manfra, M. J. Fabry-Pérot Interferometry at the
310 $\$nu=2/5\$$ Fractional Quantum Hall State. *Phys. Rev. X* **13**, 041012 (2023).

311 50. Kim, J. *et al.* Aharonov-Bohm interference and the evolution of phase jumps in fractional quantum
312 Hall Fabry-Perot interferometers based on bi-layer graphene. *arXiv.org*
313 <https://arxiv.org/abs/2402.12432v1> (2024).

314 51. Werkmeister, T. *et al.* Anyon braiding and telegraph noise in a graphene interferometer. *arXiv.org*
315 <https://arxiv.org/abs/2403.18983v2> (2024).

316 52. Samuelson, N. L. *et al.* Anyonic statistics and slow quasiparticle dynamics in a graphene fractional
317 quantum Hall interferometer. *arXiv.org* <https://arxiv.org/abs/2403.19628v1> (2024).

318

319

320

321

322

323

324

325

326

327 **METHODS**

328 **Sample preparation.** The monolayer graphene stacks with hBN and graphite encapsulation used in this study were
329 fabricated using the same polycarbonate (PC) polymer dry transfer method described in detail in our previous work
330 (Ref. 19). The graphite top-gates and bottom-gate, which encapsulate the graphene channel after stacking, are crucial
331 to screen charge disorder from the graphene channel, stabilizing robust integer and fractional QHE states at low
332 magnetic fields (Supplementary Fig. 2). The stack used for all data shown here had a top (bottom) hBN thickness of
333 49 (27) nm. After adhering the stack to a substrate and annealing in vacuum at 300°C, the top gate was first etched
334 into a simplified shape by reactive ion etching in an inductively coupled plasma etching chamber with 30W O₂ plasma
335 using a polymethyl methacrylate (PMMA) resist patterned with electron-beam lithography as the etch mask. Next, a
336 full etch through the entire stack was performed to define all outer boundaries. This etching was in several steps: first
337 a pure 30W O₂ etch remnants of the top graphite; then a 30W process O₂/CHF₃ to etch through the underlying hBN,
338 graphene, and hBN; and finally another 30W O₂ etch to remove the bottom graphite. Next, edge contacts to the exposed
339 graphene were made by a 30W CHF₃ etch on the exposed hBN/graphene/hBN contact regions and thermal evaporating
340 2/7/150 nm of Cr/Pd/Au at an angle with rotation. Then, air bridge contacts were made to the top-graphite in various
341 locations using a bilayer PMMA process followed by a short 20-25s 30W O₂ plasma PMMA residue clean and thermal
342 evaporation of 2/7/350 nm Cr/Pd/Au. Then, to etch the ~100 nm width trenches to separate the top graphite regions,
343 a thinner PMMA resist was used and again a reactive ion etch with gentle 30W O₂ plasma alone was done in ~1 minute
344 steps. In between etches, the two-probe resistance between each bridge-contacted gate was checked until they were
345 all separated. Finally, bridge contacts to the separated central hexagon gate and suspended bridges over the QPC
346 regions were deposited. See Supplementary Fig. 1 for more details on the fabrication process and the final device.

347

348 **Measurements.** The 8 top graphite gates in the device were separately controlled to set filling factors in each region
349 at perpendicular magnetic field B , since Landau level filling factor (also simply called ‘filling’) $\nu \equiv n_e/n_\phi$, where
350 $n_\phi = eB/h$ and n_e is the areal electron density. At the region in the middle of the top-gate split-gates, where the
351 graphite is etched away for a separation of ~150 nm, the electrostatics are tuned to create a saddle-point potential at
352 the QPC. See Supplementary Section 1 for details of this tuning process. Once an approximate saddle-point is formed
353 at the QPCs using the graphite top-gates and bottom-gate, the suspended metal bridges over the QPCs are tuned to
354 precisely set transmissions T_{QPC1} and T_{QPC2} . The neighboring top-gates screen out stray fields generated by the

355 suspended bridges such that V_{QPC1} and V_{QPC2} are primarily coupled to the graphene at the saddle-point of the QPCs.
356 We interpret non-integer values $0 < T_{QPC} < 1$ as a transmission probability for electrons in the outer EC, which is
357 partially transmitted, while for $1 < T_{QPC} < 2$, $T_{QPC} - 1$ gives the transmission probability for the inner EC.

358 Experiments were performed in an Oxford wet dilution system with base temperature ~ 20 mK and estimated
359 $\sim 20\text{-}25$ mK electron temperature. The 24 DC measurement lines of the fridge were carefully thermalized through
360 Thermocoax cables and 3 Sapphire plates between room temperature and the mixing chamber. A series of lumped
361 element Pi and RC filters at the mixing chamber reduced electronic noise and ensured low electron temperature. Unless
362 otherwise noted, a constant 6T perpendicular magnetic field was applied. Measurements were taken using standard
363 low-frequency lock-in amplifier techniques with a typical AC excitation current of 1 nA at 17.77 Hz applied to the
364 sample and simultaneously measured AC voltage drops and drained current. Graphite and suspended bridge gates
365 were controlled with a house-made, low-noise 16-bit D/A voltage source. Bias dependence (see Supplementary
366 Section 4) was taken by voltage biasing instead and adding in a DC bias at the source. Simultaneously, the DC voltage
367 drop V_D was measured on the same probes measuring the AC conductance so that the accurate voltage drop across the
368 FP cavity was known. All data collected and analysis programs have been made available.

369

370 **Estimation of the coupling strength.** Although we have not attempted a detailed calculation of the coupling constants
371 important for our analysis, we can at least advance some qualitative arguments for the trend that emerges from our
372 analysis. The edge of the sample consists of alternating compressible and incompressible stripes whose width is set
373 by electrostatics⁶. ECs are located in compressible stripes. It may be expected that the outermost EC is located along
374 an electron density contour where the local Landau-level filling factor is ~ 0.5 , while the second EC is located along
375 a contour with filling ~ 1.5 . Due to residual disorder and electron-electron interactions, the Hall plateau at $\nu = 2$ will
376 set in when the bulk filling is smaller than 2, though larger than 1.5. The density profile produced by charges on
377 confining gates should be relatively smooth, so that the spatial separation between the outer most EC and the second
378 EC should be relatively large at this point, and the Coulomb coupling between the channels, screened by the gates,
379 should be relatively weak. As the electron density is increased, the inner EC should move closer to the outer edge, and
380 the coupling should become stronger, and it is plausible that by the time the device enters the $\nu = 3$ plateau, the value
381 of K_{12}/K_1 is close to 1.

382 Further increases in the density should produce additional ECs, which are totally reflected at the QPCs and
383 do not contribute directly to the transport. The number of electrons on any additional closed ECs, as on other localized
384 states, will be restricted to integer values, and in principle, due to Coulomb interactions, there should be a jump in the
385 interference phase of outer edge states each time this integer changes by one. However, Coulomb interactions in our
386 system are strongly screened by the nearby gates, so if the additional channels are not close to the outer two ECs, the
387 jumps would be too small to be observable. In monolayer graphene, the energy gap at $\nu = 2$, which is due to the
388 cyclotron energy, is much larger than the gaps at $\nu = 1, 3, 4$, and 5, which arise from electron-electron interactions.
389 Consequently, we expect that the spatial separation between the outermost EC and the second EC will tend to be small
390 compared to the separation between the second EC and any additional ECs.

391 Another issue is the stability criterion embodied in the requirement $|K_{12}|^2 \leq K_1 K_2$. This requirement is
392 automatically satisfied if we assume that when the two outer ECs are close together, the energy for adding an electron
393 to either one of them is dominated by an electrostatic energy that depends primarily on the total charge on the edges,
394 and only weakly on the difference between them, so that $E = a \delta Q_1^2 + b \delta Q_2^2 + 2K_{12}(\delta Q_1 + \delta Q_2)^2$, with a and b
395 small compared to K_{12} . Then, K_1 and K_2 will be approximately equal to each other and slightly larger than K_{12} .

396 This analysis is compatible with experiments in GaAs interferometers where the ECs occur at the boundary
397 between two QHE states of different integer filling fractions (Ref. 27). There it was found that the $h/2e$ periodicity
398 occurred only if the outer EC and second EC belong to the same orbital Landau level, and not if they belong to different
399 levels. In the first case, the energy gap for the QHE state between the two ECs will arise from electron-electron
400 interactions, while the energy gap in the second case will be dominated by the generally larger cyclotron energy.
401 Therefore, in the first case, when the density is increased enough to populate a third QHE state in the bulk of the
402 sample, the two outer ECs might be pushed so close to each other that they are strongly coupled, while this might not
403 be expected to happen in the second case.

404
405 **Physics of AB frequency doubling at strong coupling.** The meaning of the charge fluctuations δQ_1 and δQ_2 can be
406 made more precise as follows. As stated in the main text, we define Q_1 as the number of electrons in the lowest spin-
407 split Landau level enclosed by the outer edge mode and Q_2 as the number of electrons in the higher spin state enclosed
408 by the inner mode. These charges are related to the enclosed areas A_1 and A_2 by $Q_i = A_i B / \Phi_0$, where $i = 1$ or 2.
409 These areas are allowed to deviate slightly from the ideal areas \bar{A}_i , which are assumed to be smooth functions of V_{PG}

410 and, at most weakly varying functions of B and V_{MG} . Then $\delta Q_i = Q_i - B\bar{A}_i/\Phi_0$, and the energy E may be expanded
411 to quadratic order in δQ_i as stated above.

412 When the inner mode is completely reflected at the QPC, the charge Q_2 is constrained to be an integer, while
413 the charge Q_1 can change continuously, assuming that the outer edge is mostly transmitted through the QPCs. At low
414 temperatures the charges will be determined so as to minimize E , subject to the integer constraint.

415 If Q_2 is held fixed while the magnetic field is increased by a small amount dB , the inner edge charge δQ_2
416 will change by an amount $-dB\bar{A}_2/\Phi_0$. This happens because, as the area shrinks, charge is transferred from the edge
417 region to the interior, where it is effectively screened by the gates, leaving a charge deficit at the edge. In the strong
418 coupling limit, this will cause δQ_1 to increase by an equal amount. Thus, the total charge Q_1 in the lowest spin-split
419 Landau level will increase by $dQ_1 = dB(\bar{A}_1 + \bar{A}_2)/\Phi_0$, and the interferometer phase θ will increase by $2\pi dQ_1$.

420 If B is increased by a large amount, the value of Q_2 will not be fixed but will undergo periodic integer jumps.
421 In the strong coupling limit, the jump in Q_1 caused by a jump in Q_2 will also be an integer. This will cause θ to jump
422 by a multiple of 2π , which will be invisible in an interferometer experiment. Thus, the observed rate of change of the
423 phase will be $d\theta/dB = 2\pi(\bar{A}_1 + \bar{A}_2)/\Phi_0$, which is equal to $4\pi\bar{A}_1/\Phi_0$, if we neglect the difference between \bar{A}_1 and
424 \bar{A}_2 . This rate of change is twice as fast as would have been observed in the absence of coupling between the inner and
425 outer edge modes.

426 We remark that in the course of adding one flux quantum to the area \bar{A}_1 , one would expect on average to have
427 a jump by one electron in each spin state. So, in general, one will have one positive jump in Q_2 and one negative jump
428 in Q_1 . Thus, while the observed interference phase will change by an amount equivalent to a change of two electrons,
429 the actual change in Q_1 will only be one electron.

430

431 **Robustness of the theoretical predictions.** As discussed in Ref. 36, when a single EC passes through the two
432 constrictions, with weak backscattering at the constrictions, the interference phase seen at low temperatures and low
433 source-drain voltage is given by $\theta = 2\pi Q + \theta_0, \text{mod } 2\pi$, where Q is the total electron charge (in units e) in the region
434 between the two scattering points (the expectation value of the charge on the interferometer in its ground state) and
435 θ_0 is a constant for small variations in B , V_{PG} , and V_{MG} . The argument is essentially the same if the backscattering is
436 not weak. The principal effect of stronger backscattering at the QPCs is to add a term to the energy E that favors
437 integer values of the charge Q_1 and hence integer values of the total charge on the interferometer. This means that as

438 the control parameters are varied continuously, the phase difference $\theta - \theta_0$ will undergo an additional modulation
439 pulling it towards the nearest integer multiple of 2π . If we define θ_b as the value of the interferometer phase that
440 would occur in the limit of weak backscattering, for the given value of the control parameters, then the actual value
441 of θ should have the form $\theta = \theta_b + \delta\theta$, where $\delta\theta$ is a periodic function of $\theta_b - \theta_0$. In addition, in the presence of
442 finite back scattering, interference contribution to the measured resistivity may no longer be a simple sinusoidal
443 function of θ but can contain higher harmonics. The combination of these effects means that the interference current
444 will remain a periodic function of θ_b , with period 2π , but the relative amplitudes of various harmonics may be
445 modified. In the main text, it was argued that $\cos \theta_b$ should be a two-dimensional periodic function of B and the gate
446 voltages, with frequencies expressed in terms of two non-colinear fundamental vectors in reciprocal parameter space.
447 The effect of finite backscattering at the QPCs will be to modify the amplitudes of the various Fourier components,
448 but not to change their positions.

449 Using similar arguments, we may argue that measurement at finite temperature should not change the
450 locations of the fundamental frequency vectors, but thermal fluctuations will reduce the Fourier amplitudes. In general,
451 at high temperatures T , the amplitude of a given Fourier component will fall off, proportional to $e^{-T/\varepsilon}$, where ε will
452 be different for each Fourier component. At sufficiently high temperatures, therefore, only the one or two components
453 with the largest values of ε will remain visible. The values of ε will depend on details of the system, but typically the
454 Fourier components that are most prominent at $T = 0$ will be the ones that persist to highest temperatures.

455 For our system, in the case where there is only a single EC, as we find for bulk filling less than 2, the value
456 of ε for the lowest Fourier mode is predicted to be $\varepsilon = h\nu/(2\pi^2 P)$, where ν is the EC velocity and P is the perimeter
457 of the interferometer path. For the case of two strongly coupled edge channels, the prediction is $\varepsilon = h\nu/(4\pi^2 P)$,
458 where ν is now the velocity of the fast charge mode. In both cases, the dominant effects come from thermal fluctuations
459 $e\delta Q$ of the charge on the edge, whose energy cost is given by $(e\delta Q)^2/(2\gamma P)$, where γ is the capacitance per unit
460 length of the edge. The velocity ν is given by $\nu = \delta\sigma_{xy}/\gamma$, where $\delta\sigma_{xy}$ is the change in Hall conductance across the
461 edge. Using our lithographically defined perimeter $P = 4.24 \mu\text{m}$ and the velocity $v_e = \frac{e\Delta V_D P}{h} = 1.46 \times 10^5 \text{ m/s}$
462 extracted from finite-bias dependence in the uncoupled case (SI), we find $\varepsilon = 83.7 \text{ mK}$, well above our estimated
463 electron temperature.

464

465

466 **Acknowledgements**

467 We thank Andrew Pierce and Raymond Ashoori for helpful comments in the early stages of this work. We also thank
468 Raymond Ashoori for lending important cryostat parts used in this measurement and Jim MacArthur for building
469 electronics used in our experiment. P.K., T.W., and Y.R. acknowledge support from DOE (DE-SC0012260) for sample
470 preparation, measurement, characterization, and analysis. J.R.E. acknowledges support from ARO MURI (N00014-
471 21-1-2537) for sample preparation, measurement, characterization, and analysis. K.W. and T.T. acknowledge support
472 from the Elemental Strategy Initiative conducted by the MEXT, Japan, Grant Number JPMXP0112101001, JSPS
473 KAKENHI Grant Number JP20H00354 and the CREST(JPMJCR15F3), JST. D.E.F. and Z.W. acknowledge support
474 by the National Science Foundation under Grant No. DMR-2204635. B.I.H. acknowledges support from NSF grant
475 DMR-1231319. Nanofabrication was performed at the Center for Nanoscale Systems at Harvard, supported in part by
476 an NSF NNIN award ECS-00335765.

477

478 **Author contributions**

479 T.W. and D.N. stacked the graphite-encapsulated heterostructures. T.W. performed the nanofabrication, measurements,
480 and data analysis. J.R.E. and Y.R. assisted in the measurement and analysis. D.E.F., B.I.H., and Z.W. contributed the
481 theoretical analysis. M.E.W. and A.Y. provided the measurement cryostat and collaborated on the discussions and
482 analysis. K.W. and T.T. provided the hBN crystals. T.W., B.I.H., J.R.E., and P.K. wrote the paper with input from all
483 authors.

484

485 **Competing interests**

486 The authors declare no competing interests.

487

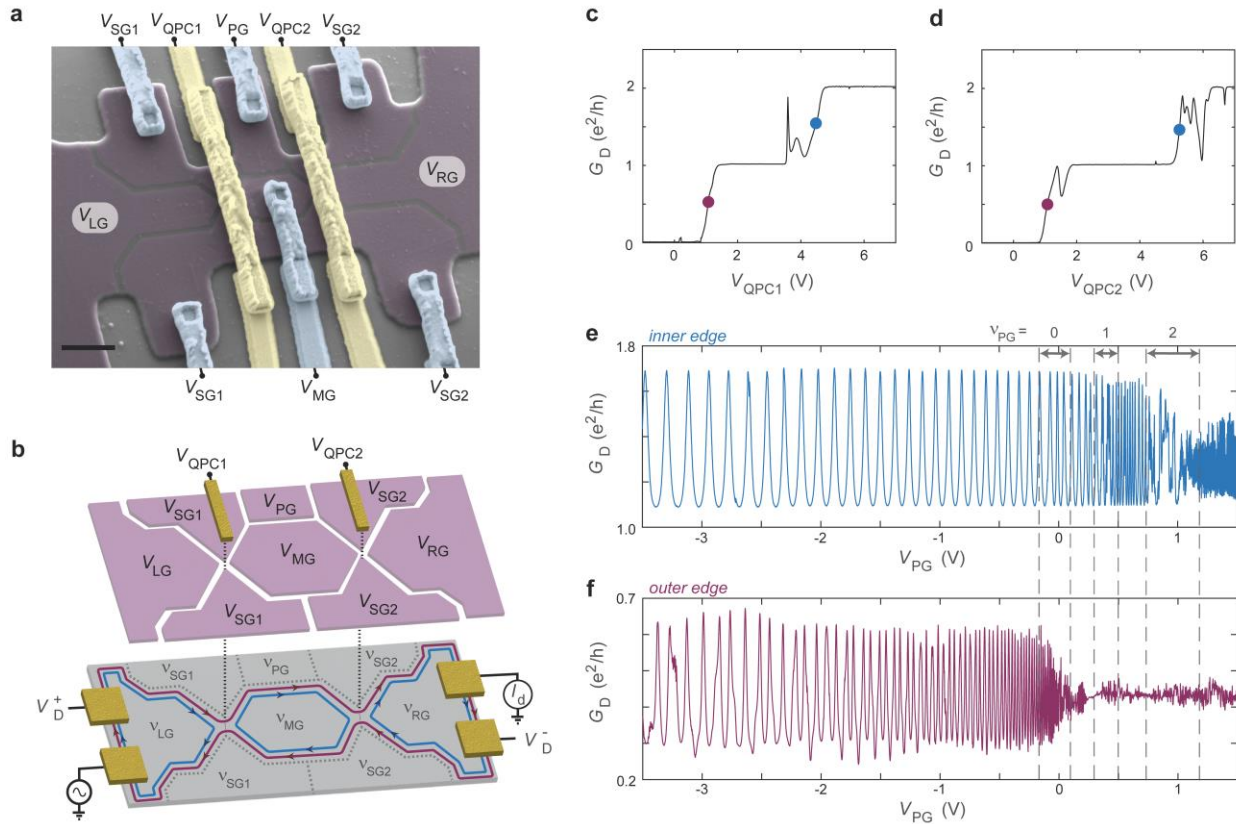
488

489

490

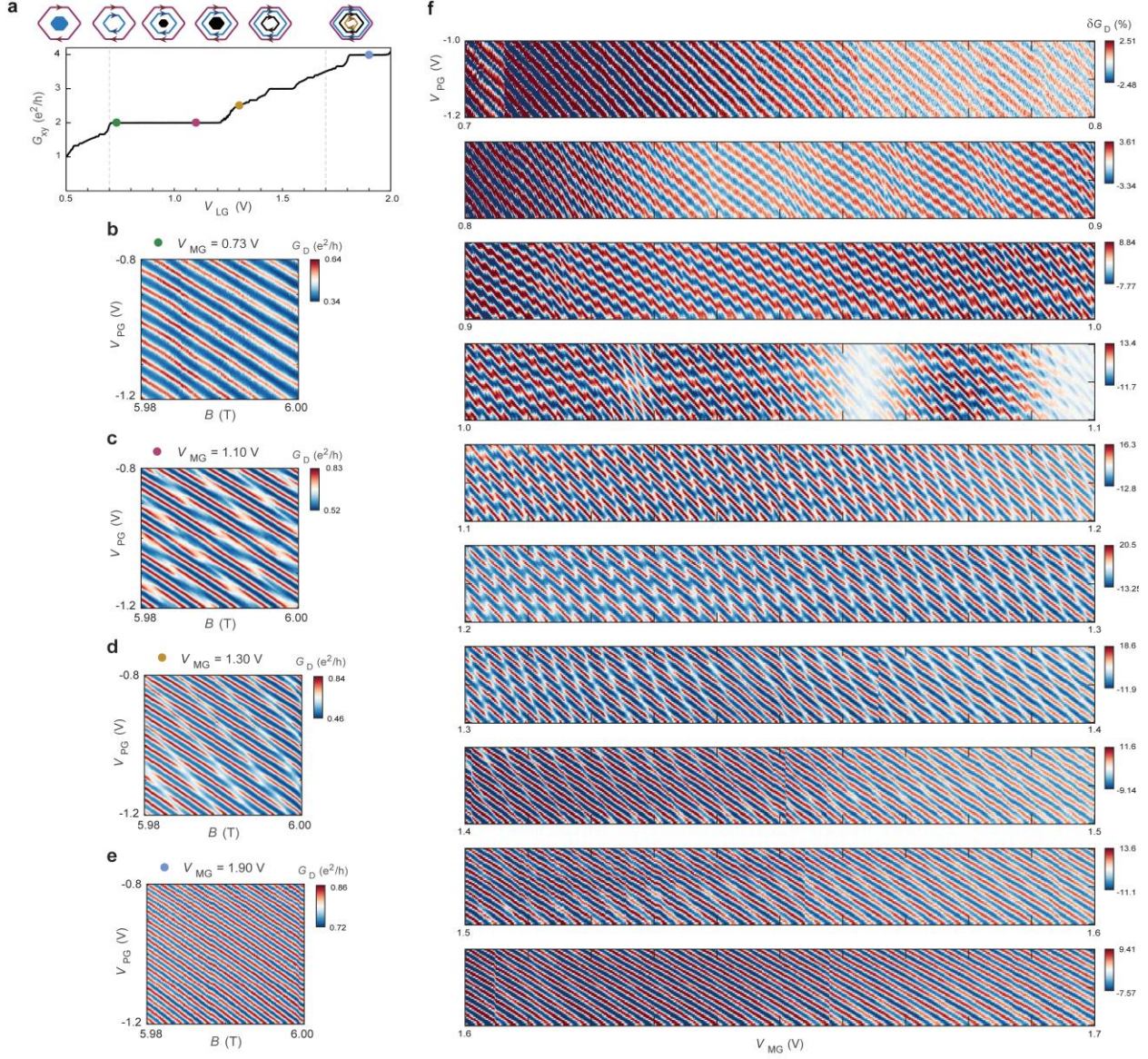
491

492

493 **FIGURES**

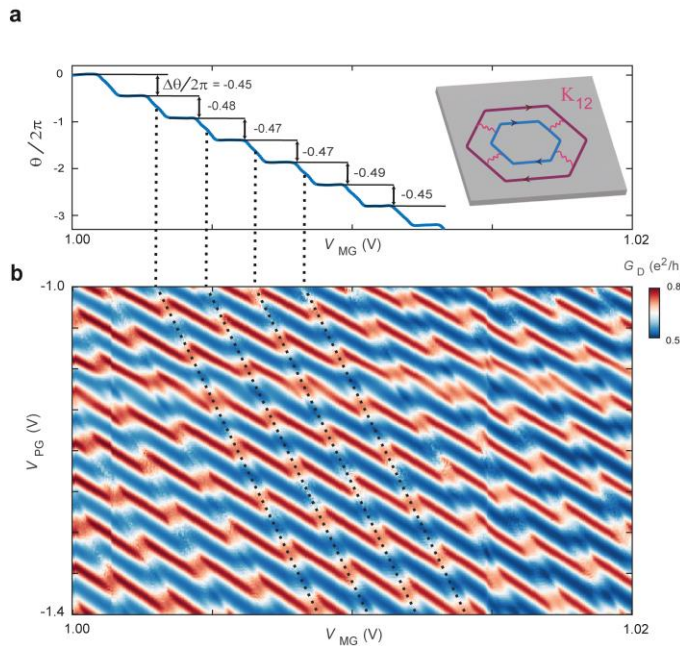
494

495 **Figure 1. Highly tunable Fabry-Pérot interferometer in graphene.** **a**, False-colour scanning electron microscopy
 496 image of a FP device identical to the device measured here. The graphite top-gate layer is selectively etched to form
 497 8 separated top-gates (purple). Metal bridges (blue) connect to each graphite top-gate region and two additional bridges
 498 (yellow) suspend over the QPCs. The lithographic area of the interferometer cavity (area $A = 1.16 \mu\text{m}^2$) is defined
 499 by the central hexagonal top-gate. Scale bar: 1 μm . **b**, Simplified schematic of a FP tuned so that $V_{\text{LG}} = V_{\text{MG}} = V_{\text{RG}} = 2$ and $V_{\text{SG1}} = V_{\text{PG}} = V_{\text{SG2}} = 0$ illustrating interference of the partitioned outer EC (red) while the inner EC (blue) forms a closed annulus inside the FP. Voltages applied to the suspended metal bridges V_{QPC1} and V_{QPC2} selectively gate the QPC constrictions through the etched graphite gaps. We measure the diagonal conductance $G_{\text{D}} = I_{\text{d}}/(V_{\text{D}}^+ - V_{\text{D}}^-)$, where V_{D}^{\pm} and I_{d} are measured voltages in (\pm) probes and drained current, respectively. See
 504 Supplementary Fig. 1 for the full device geometry and additional details. In addition to magnetic field, we tune the
 505 interference phase using voltage V_{MG} on the ‘middle gate’ or V_{PG} on the ‘plunger gate’. **c**, Conductance as a function
 506 of V_{QPC1} with $V_{\text{QPC2}} = 7$ V (i.e. open with $T_{\text{QPC2}} = 2$) demonstrating QPC1 tunings to interfere outer EC (red dot) and
 507 inner EC (blue dot) in $\nu = 2$. **d**, Same type of plot as **c**, but demonstrating QPC2 operation instead of QPC1. See
 508 Supplementary Fig. 3 for QPC tuning details and voltages set on the other gates to form the necessary QPC saddle-
 509 points to acquire this data. **e-f**, Characteristic FP oscillations as a function of V_{PG} for the inner EC and outer EC,
 510 respectively, at the indicated QPC tunings. All data is at fixed magnetic field $B = 6$ T.

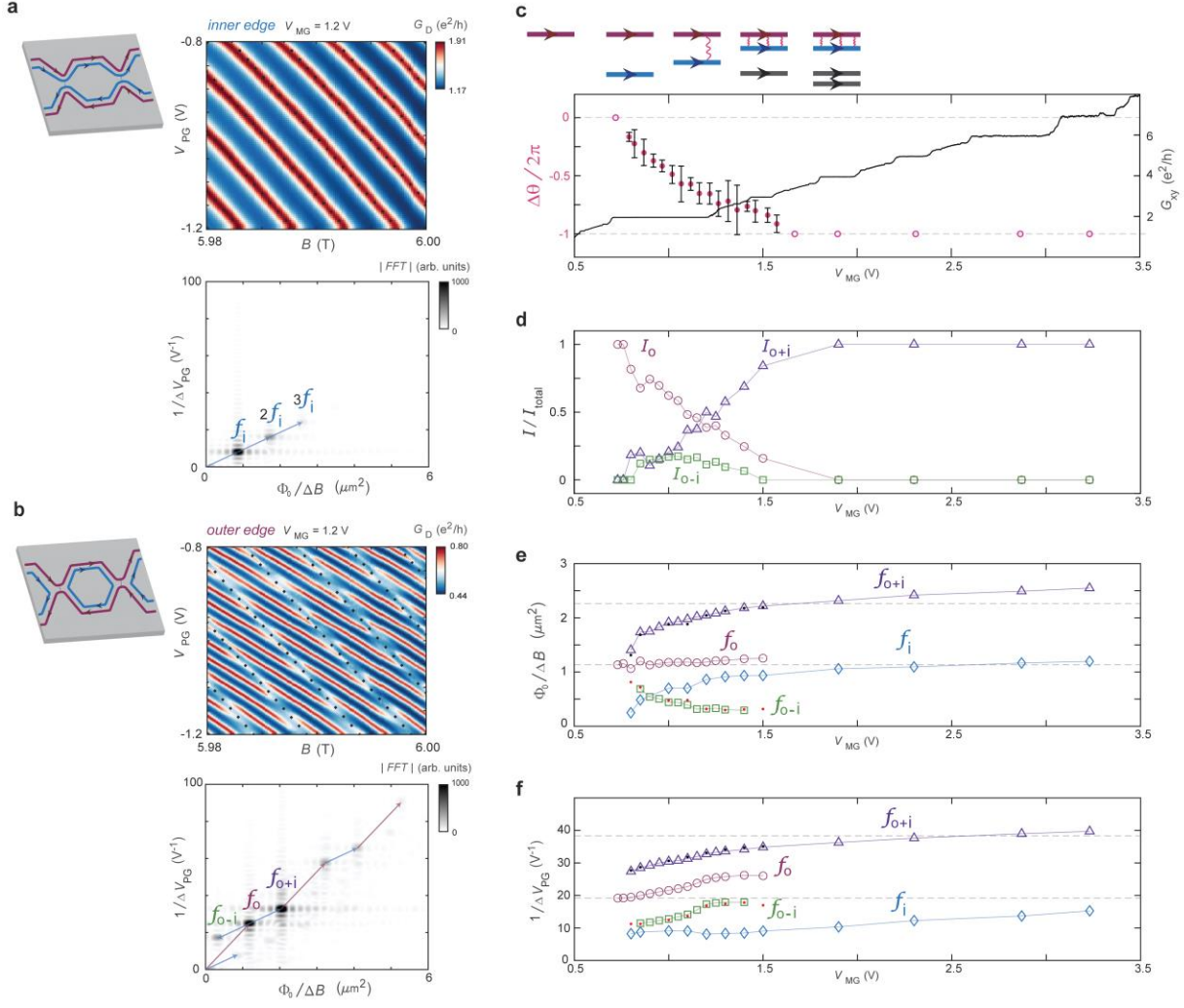


511

512 Figure 2. **Density-tuned AB oscillation frequency doubling transition of outer EC.** a, Hall conductance G_{xy} of the
 513 device with both QPCs tuned to be fully open, demonstrating that V_{MG} tunes the filling ν of the FP at a fixed magnetic
 514 field $B = 6$ T. Colored dots indicate points at which interference data are shown in b-e while vertical dashed lines
 515 show the range of V_{MG} swept for f. Top inset pictures illustrate the corresponding compressible regions expected in
 516 the FP cavity. b-e, Conductance G_D oscillations on the outer EC with V_{PG} and B , for each of the indicated V_{MG} values.
 517 f, Conductance G_D oscillations on the outer EC with V_{PG} and V_{MG} , for V_{MG} swept continuously over the transition from
 518 apparent h/e to $h/2e$ oscillations periodicity, at $B = 6$ T. Here we plot G_D as a percentage of $\frac{e^2}{h}$ deviation from the
 519 average value, which is calculated for each fixed V_{MG} linecut and subtracted off. QPCs are retuned to maintain $T_{QPC1} =$
 520 $T_{QPC2} = 0.5$ over the dataset. We do not observe further phase jumps or periodicity changes past $V_{MG} \approx 1.7$ V (checked
 521 up to $V_{MG} = 3.2$ V, corresponding to $\nu = 7$).



524 **Figure 3. Phase jump extraction in the transition regime.** **a**, Phase of the 1D fast Fourier transform (FFT) extracted
 525 along linecuts parallel to the phase jumps in **(b)**. The phase is evaluated at the dominant frequency in the FFT amplitude
 526 spectrum for the linecuts in between phase jumps. A linear increase in phase extracted from the regions without phase
 527 jumps is subtracted off to make the phase jump magnitude evident as the vertical shift between plateaus in panel (a).
 528 From this data we extract $\Delta\theta/2\pi \approx -0.47$, reflecting approximately half of an electron repelled from the outer EC
 529 for each charge added to Q_2 . Inset: illustration of the coupling K_{12} between the outer and inner ECs contributing to
 530 the phase jumps. **b**, Conductance G_D oscillations on the outer EC with V_{PG} and V_{MG} near the center of the transition
 531 regime showing periodic phase jumps along the dashed black lines. Note that increasing V_{MG} adds electrons to the
 532 system or equivalently increases phase, so the phase jumps correspond to negative shifts in phase i.e., repulsion of
 533 electrons from the FP cavity. [Similar interference patterns are observed in both the strong and weak QPC](#)
 534 [backscattering regimes \(Supplementary Fig. 4\)](#) as well as at elevated temperatures (Supplementary Fig. 5).



536

537 **Figure 4. Comparison of inner and outer EC interference and couplings across transition.** **a**, Conductance G_D
 538 oscillations on the inner EC ($T_{QPC1} = T_{QPC2} = 1.5$) with V_{PG} and B , for $V_{MG} = 1.2V$. Left: illustration of interference
 539 on inner EC. Bottom: 2D FFT of the G_D oscillations showing peak f_i and its harmonics. **b**, Same analysis and V_{MG}
 540 value as in **(a)** but for interference on the outer EC ($T_{QPC1} = T_{QPC2} = 0.5$), showing the peaks f_o , f_{o+i} , and f_{o-i} and
 541 their harmonics. **c**, Magnitude of the phase jump (obtained using the method shown in Fig. 3) as a function of V_{MG} ,
 542 showing that it is continuously tunable. Each data point is averaged over ~ 0.25 V range in V_{MG} and error bars indicate
 543 ± 1 standard deviation over the phase jumps detected in this range. Unfilled data points represent zero observable
 544 phase jumps over the corresponding V_{MG} range, hence we infer a magnitude of 0 or -1 . **We show G_{xy} of the device**
 545 **taken in an identical measurement to Fig. 2a, reflecting the expected V_{MG} , for reference.** **d**, Normalized magnitudes
 546 I_o , I_{o+i} , and I_{o-i} of the respective peaks f_o , f_{o+i} , and f_{o-i} obtained as a function of V_{MG} . I_o , I_{o+i} , and I_{o-i} are
 547 normalized by the sum $I_o + I_{o+i} + I_{o-i}$ to show their relative contributions. We extract each data point from a 2D
 548 dataset like panel **(b)**, a subset of which are shown in [Supplementary Fig. 7](#). **e**, **Magnetic field frequency multiplied**
 549 **by $\Phi_0 \equiv h/e$** for peaks f_o , f_i , f_{o+i} , and f_{o-i} tracked through the transition. Note that f_i is measured from a separate
 550 measurement of interference on the inner EC ([Supplementary Fig. 8](#)), while the other peaks are all extracted from
 551 interference on the outer EC. **f**, Same as **(e)** but for plunger gate frequency. Horizontal dashed lines in **(e-f)** indicate
 552 the corresponding f_o and $2f_o$ values before the transition. Black (red) dots show calculated $f_o \pm f_i$ from outer and
 553 inner EC data, which match the peaks identified as f_{o+i} and f_{o-i} , respectively.